Dieless bulging and nonlinear buckling of longan-shaped pressure hull

He, Rui; Zhang, Jian; Kaewunruen, Sakdirat; Zhan, Ming; Liu, Ping

DOI:
10.1016/j.ijnaoe.2023.100548

Document Version
Publisher's PDF, also known as Version of record

Citation for published version (Harvard):
He, R, Zhang, J, Kaewunruen, S, Zhan, M & Liu, P 2023, 'Dieless bulging and nonlinear buckling of longan-shaped pressure hull', *International Journal of Naval Architecture and Ocean Engineering*, vol. 15, 100548. https://doi.org/10.1016/j.ijnaoe.2023.100548

International Journal of Naval Architecture and Ocean Engineering 15 (2023) 100548

Contents lists available at ScienceDirect

International Journal of Naval Architecture and Ocean Engineering

journal homepage: http://www.journals.elsevier.com/international-journal-of-naval-architecture-and-ocean-engineering/

Dieless bulging and nonlinear buckling of longan-shaped pressure hull

Rui He [a], Jian Zhang [a, *], Sakdirat Kaewunruen [b], Ming Zhan [a], Ping Liu [c]

[a] School of Mechanical Engineering, Jiangsu University of Science and Technology, Zhenjiang, China
[b] Department of Civil Engineering, School of Engineering, University of Birmingham, Birmingham, UK
[c] School of Civil Engineering, Jiangsu University of Science and Technology, Zhenjiang, China

ARTICLE INFO

Article history:
Received 22 February 2023
Received in revised form
25 July 2023
Accepted 21 August 2023
Available online 28 August 2023

Keywords:
Longan-shaped geometry
Pressure hull
Dieless bulging
Buckling behavior

ABSTRACT

In this study, the dieless bulging and nonlinear buckling behaviours of a stainless longan-shaped pressure hull were investigated. According to the Cassini oval equation, the longan shape has a shape index of 0.1. The lengths of the major and minor axes of the designed longan-shaped pressure hull were approximately 400 and 396 mm, respectively. The wall thickness of this pressure hull was 1 mm. The Huber–von Mises stress and first yielding load of the designed longan-shaped shell and its inscribed polyhedral preform were investigated analytically and experimentally. Moreover, the dieless bulging of the designed longan-shaped pressure hull was investigated numerically and experimentally by using the nonlinear finite element method and a hydrostatic test, respectively. The analytical, experimental, and numerical results exhibited good agreement with each other.

1. Introduction

Pressure hulls have attracted considerable research interest for their use in underwater applications (Zoelly, 1915). Generally, pressure hulls are shells of revolution that are subjected to uniform external pressure. They are widely used in underwater facilities, such as torpedoes (Kohnen, 2009), underwater observatories (Zingoni and Enoma, 2020), submarines (Kohnen, 2009), and submersibles (Błachut, 2010). The most widely used pressure hull geometries include spheres (D. Liu et al., 2022; Pan and Cui, 2010, 2011; Zhang et al., 2017b), cylinders (Błachut, 2015; Cerik et al., 2013; Fu et al., 2023; Ifayefunmi, 2016; Li et al., 2017; Zhang et al., 2021e), cones (Błachut, 2013, 2011; Ifayefunmi and Błachut, 2013), and combinations of these shapes. Atypical shells, such as ellipsoidal shells (Li et al., 2019; Ma et al., 2008; Tang et al., 2023; Zheng et al., 2020), toroidal shells (Enoma and Zingoni, 2020; Zhang et al., 2021b, 2021d), egg-shaped shells (Zhang et al., 2018a, 2021a, 2022b), barrel-shaped shells (Magnucki and Jasion, 2013; Zhang et al., 2021c, 2022d), and Cassini oval shells (Malinowski and Belica, 2017; Sowiński and Jasion, 2019; Tang et al., 2019; Zhang et al., 2018, 2018b), are used in various applications. However, these structures are susceptible to buckling under hydrostatic pressure, whose effects on a pressure hull depend on its shape, material properties, and initial geometrical imperfections. (Arbocz and Starnes, 2002; Błachut, 2014; Thompson, 2015; Zingoni, 2015).

Classical mechanics indicates that a sphere is the optimal geometry for underwater pressure hulls (Timoshenko et al., 1962). Therefore, spherical pressure hulls are the most widely used pressure hulls. However, studies have indicated that spherical pressure hulls have a high initial imperfection sensitivity (CCS, 2014; Cui, 2013; Cui et al., 2014; Pan et al., 2012, 2010; Zhang et al., 2018c). This negative characteristic not only results in a high manufacturing cost for spherical hulls but also causes considerable difficulty in accurately predicting the buckling pressure of these hulls. To reduce the influence of imperfection sensitivity on the buckling behavior of shells, atypical hull geometrics have been widely investigated. On the basis of the results obtained for Cassini oval shells by Jasion and Magnucki (2015), Zhang et al. (2018b) conducted a numerical and experimental study of the elastic buckling of externally pressurised Cassini oval shells with various shape indices; these shells were made of photosensitive resin. Zhang et al. found that the critical buckling load of a Cassini oval shell with a shape index of 0.1, which was similar to a sphere, was much higher than that of a spherical shell because of the effects of imperfection sensitivity, circumferential radius, and meridional radius. The subsequent research indicated that Cassini oval shells are a promising geometry for pressure hulls (Zhang et al., 2018). However, the manufacture of pressure hulls with a Cassini oval shape is challenging. Zhang et al. (2018b) only focused on the

* Corresponding author.
E-mail address: zhjian127@163.com (J. Zhang).
Peer review under responsibility of The Society of Naval Architects of Korea.

https://doi.org/10.1016/j.ijnaoe.2023.100548

buckling behaviour of Cassini oval shells, and researchers have paid little attention to methods for manufacturing pressure hulls.

Dieless bulging is an alternative method for manufacturing longan-shaped pressure hulls. Compared with traditional manufacturing methods, Dieless bulging technology has the advantages of low manufacturing cost, short production time, and simple equipment. This technology has been widely investigated and used to manufacture shells of revolution (Hu and Wang, 2004; Yuan et al., 2013; Yuansong et al., 1997; Zhang and Yuan, 2016). For example, Wang et al. (2005) investigated the free hydroforming performance of spherical shells. Yuan et al. (2015) investigated the hydroforming of prolate and oblate ellipsoids by using theoretical, numerical, and experimental methods. They proposed double generating lines and reverse geometric models for the preform to manufacture objects with a sound ellipsoidal geometry. The aforementioned authors theorised that any geometry can be bulged into a sphere (Yuan et al., 2015; Zhang et al., 2015). However, their studies have only focused on decorative work and internal pressure vessels. Therefore, other researchers have investigated the hydroforming and buckling behaviour of external pressure hulls, including egg-shaped (Zhang et al., 2022a, 2022b), barrel-shaped (Zhang et al., 2022d) and toroid-shaped (X. Liu et al., 2022; Zhang et al., 2022c) pressure hulls, by using theoretical, numerical, and experimental methods. These researchers have investigated not only the hydroforming processes but also the buckling behaviours of egg-, barrel-, and toroid-shaped pressure hulls. Inspired by the aforementioned research, the dieless bulging and nonlinear buckling performance of a longan-shaped pressure hull were investigated in the present study.

The rest of this paper is organised as follows. Section 2 defines the geometries and material of a longan-shaped shell and its polyhedral preform. A set of analytical formulas were used to analyse the geometrical and mechanical properties of both the aforementioned structures. Section 3 details the methodologies used to manufacture the longan-shaped polyhedral preform, conduct the bulging and buckling tests, and shape and thickness measurements. Section 4 describes the numerical analysis conducted for examining the bulging and buckling performance of the aforementioned structures. Moreover, it presents a comparison of the numerical, analytical, and experimental results obtained in this study. Finally, section 5 provides the conclusions of this study.

2. Problem description

This section details the geometric parameters, Huber–von Mises stresses, and first yielding loads of the longan-shaped polyhedral preform and longan-shaped pressure hull. The material properties of the stainless steel used to manufacture the longan-shaped polyhedral preform are also mentioned.

2.1. Geometry and material

We considered that a longan-shaped pressure hull can be manufactured from a longan-shaped polyhedral preform by using dieless bulging technology. The nominal geometries of the longan-shaped pressure hull and longan-shaped polyhedral preform are depicted in Fig. 1. The longan-shaped pressure hull has a major axis (L), minor axis (B), and uniform wall thickness (t_1). This hull has a parallel circle radius of Y_1 and is subjected to a uniformly distributed external pressure, P_1. The longan-shaped polyhedral preform has a uniform wall thickness of t_2 , a circumferential radius of X_2 and parallel circle radius of Y_2 and is subjected to a uniformly distributed external pressure, P_2. The preform includes eight cone segments and nine segmentation points. The meridional radius of the longan-shaped pressure hull can be expressed using geometric functions in the two-dimensional Cartesian coordinate system as follows:

$$Y_1 = \pm\sqrt{\sqrt{4c^2x^2 + a^4} - c^2 - x^2}, x \in [-200, 200] \tag{1}$$

Moreover, the meridional radius of the longan-shaped polyhedral preform can be expressed as follows:

$$Y_2 = k_i x + b_i, i = 1, 2, 3 \ldots 8 \tag{2}$$

where

$$k_i = \frac{y_{i+1} - y_i}{x_{i+1} - x_i} \tag{3}$$

$$b_i = \frac{x_{i+1}y_i - x_i y_{i+1}}{x_{i+1} - x_i} \tag{4}$$

The terms a and c denote equation parameters, i is the identifier of a cone numbered from the top plate to the base plate, and α_i is the angle between the preform meridian of the i th cone segment and the major axis. The shape index ($k_c = c/a$) influences the shape of the longan-shaped pressure hull. The geometric parameters of the longan-shaped pressure hull and longan-shaped polyhedral preform are listed in Table 1.

The material properties of the stainless steel used in the experiment were determined through a uniaxial tensile test. The obtained true stress–strain curves are depicted in Fig. 2. The coupon for the uniaxial test was designed according to the GB/T 228.1–2010 (Standards Press of China, 2011) guidelines and cut from the same plate as was the longan-shaped polyhedral preform. The true stress–strain curves are nearly bilinear. The material properties were as follows: Young's modulus $(E) = 200.2$ GPa, Poisson's ratio $(\mu) = 0.299$, yield point $(\sigma_y) = 277.4$ MPa, and strength coefficient $(K) = 1307.4$ MPa. Young's modulus was determined from the slope of the linear elastic stage (first stage) of the stress–strain curves. Poisson's ratio was determined from the ratio of the transverse strain to the longitudinal strain. The yield point was calculated as 0.2% of the proof stress. Finally, the strength coefficient was determined from the slope of the linear plastic stage (second stage) of the stress–strain curves. The linear elastic stage is mathematically expressed as $\sigma = E\varepsilon$, and the linear plastic stage is mathematically expressed as $\sigma = \sigma_y + K(\varepsilon - \varepsilon_y)$, where ε_y is the yield strain $(= \sigma_y / E)$.

2.2. Analytical estimation

According to the membrane theory of shells of revolution (Ventsel, et al., 2002), the meridional stress (σ_{m1}), circumferential stress ($\sigma_{\theta 1}$), and Huber–von Mises stress (σ_{e1}) of the longan-shaped pressure hull can be determined as follows:

$$\sigma_{m1} = -\frac{P_1 Y_1 \sqrt{1 + (Y_1{}')^2}}{2t_1} \tag{5}$$

$$\sigma_{\theta 1} = \sigma_{m1}\left(2 + \frac{Y_1 Y_1''}{1 + (Y_1')^2}\right) \tag{6}$$

and

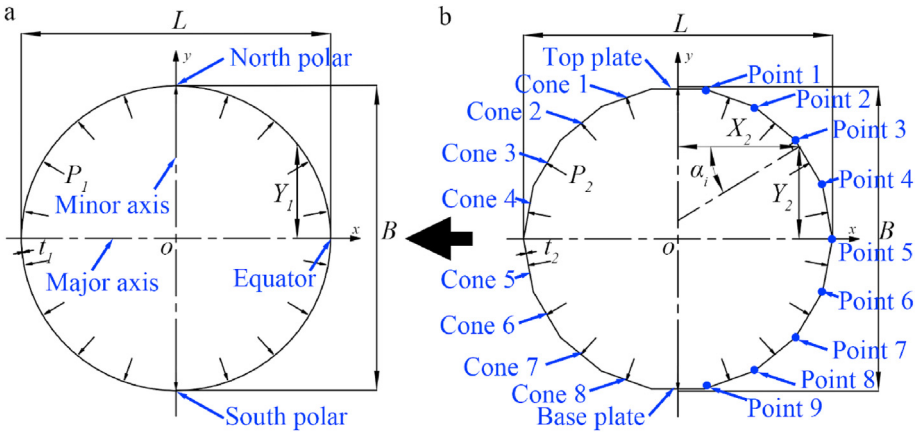

Fig. 1. Nominal geometries of the (a) longan-shaped pressure hull and (b) longan-shaped polyhedral preform.

Table 1
Geometric parameters of the longan-shaped pressure hull and longan-shaped polyhedral preform.

a [mm]	199.01
c [mm]	19.9
k_c	0.1
B [mm]	396.2
L [mm]	400
t_1 [mm]	1.055
t_2 [mm]	1.065
P_1 [MPa]	1
P_2 [MPa]	1
Point 1 (x_1, y_1)	(34.39, 195.05)
Point 2 (x_2, y_2)	(99.25, 171.91)
Point 3 (x_3, y_3)	(152.58,101.03)
Point 4 (x_4, y_4)	(187.82, 68.32)
Point 5 (x_5, y_5)	(200, 0)
Point 6 (x_6, y_6)	(187.82, −68.32)
Point 7 (x_7, y_7)	(152.58, −101.03)
Point 8 (x_8, y_8)	(99.25, −171.91)
Point 9 (x_9, y_9)	(34.39, −195.05)

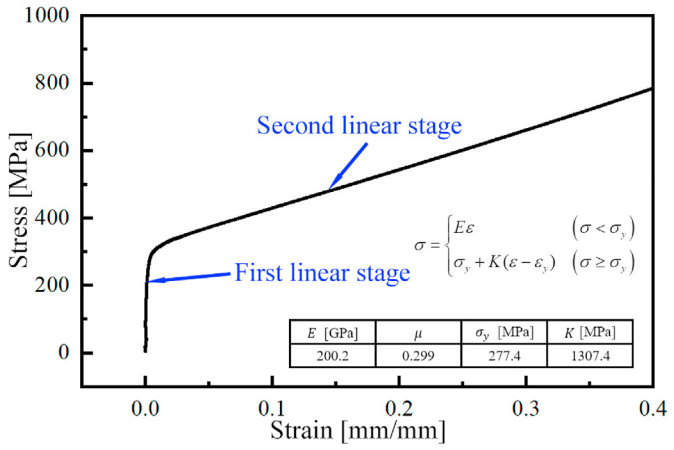

Fig. 2. True stress–strain curves determined by conducting a uniaxial tensile test on a stainless steel coupon. The coupon was designed according to the GB/T 228.1–2010 guidelines and cut from the same plate as was the longan-shaped polyhedral preform.

$$\sigma_{e1} = \sqrt{(\sigma_{m1})^2 + (\sigma_{\theta 1})^2 - \sigma_{m1}\sigma_{\theta 1}} \tag{7}$$

By substituting Eqs. (5) and (6) into Eq. (7), the following equation is obtained:

$$\sigma_{e1} = \frac{P_1 Y_1}{2t_1} \cdot \sqrt{3 + 3(Y_1')^2 - Y_1 Y_1'' + \frac{{Y_1}^2 (Y_1'')^2}{1 + (Y_1')^2}} \tag{8}$$

Assuming that the Huber–von Mises stress is equal to the material yielding point ($\sigma_{e1} = \sigma_y$), the yielding load P_{y1} of the longan-shaped pressure hull can be obtained by combining Eqs. (5)–(8) as follows:

$$P_{y1} = \frac{2t_1\sigma_y}{Y_1\sqrt{3 + 3(Y_1')^2 - Y_1 Y_1'' + \frac{{Y_1}^2 (Y_1'')^2}{1+(Y_1')^2}}} \tag{9}$$

where

$$Y_1' = \frac{2c^2x - x\sqrt{4c^2x^2 + a^4}}{\sqrt{\sqrt[3]{4c^2x^2 + a^4} - (4c^2x^2 + a^4)(c^2 + x^2)}} \tag{10}$$

and

$$Y_1'' = \frac{\left(2c^2 - \sqrt{4c^2x^2 + a^4} - \frac{4c^2x^2}{\sqrt{4c^2x^2+a^4}}\right)\sqrt{\sqrt[3]{4c^2x^2 + a^4} - (4c^2x^2 + a^4)(c^2 + x^2)}}{\sqrt[3]{4c^2x^2 + a^4} - (4c^2x^2 + a^4)(c^2 + x^2)} + \frac{-16c^4x^2 - 56c^4x^4 - 10a^4c^2x^2 + \sqrt{4c^2x^2 + a^4}(20c^4x^2 + 16c^2x^2 + 2a^4x^2)}{\sqrt{\sqrt[3]{4c^2x^2 + a^4} - (4c^2x^2 + a^4)(c^2 + x^2)}} \tag{11}$$

Similarly, the meridional stress (σ_{m2}), circumferential stress ($\sigma_{\theta 2}$), and Huber–von Mises stress (σ_{e2}) of the longan-shaped polyhedral preform can be determined as follows:

$$\sigma_{m2} = \frac{P_2 X_2}{2t_2 cos\ \alpha_i} \tag{12}$$

$$\sigma_{\theta 2} = \frac{P_2 X_2}{t_2 cos\ \alpha_i} \tag{13}$$

and

$$\sigma_{e2} = \sqrt{(\sigma_{m2})^2 + (\sigma_{\theta 2})^2 - \sigma_{m2}\sigma_{\theta 2}} \tag{14}$$

By substituting Eqs. (12) and (13) into Eq. (14), the following equation is obtained:

$$\sigma_{e2} = \frac{\sqrt{3} P_2 X_2}{2t_2 cos\ \alpha_i} \tag{15}$$

Assuming that the Huber–von Mises stress equals the material yielding point ($\sigma_{e2} = \sigma_y$), the yielding load (P_{y2}) of the longan-shaped polyhedral preform can be obtained by combining Eqs. (12)–(15) as follows:

$$P_{y2} = \frac{2t_2 \sigma_y cos\ \alpha_i}{\sqrt{3} X_2} \tag{16}$$

The final bulging load can be expressed as follows:

$$P_h \geq P_{y1} \tag{17}$$

The analytical results obtained for the Huber–von Mises stress of the longan-shaped polyhedral preform by using Eq. (13) are listed in Table 2.

The Huber–von Mises stress of the longan-shaped polyhedral preform was higher than that of the longan-shaped pressure hull. Fig. 3 depicts the Huber–von Mises stresses obtained for the pressure hull and polyhedral preform by using Eqs. (8) and (15), respectively, under internal pressure of 1 MPa. The aim of assuming the internal pressure to be 1 MPa was to obtain the variation tendency of Huber–von Mises stresses. As displayed in Fig. 3, the distributions of the Huber–von Mises stresses of the polyhedral preform and pressure hull exhibited symmetry, which can be attributed to the fact that both structures are symmetric. The Huber–von Mises stress of the polyhedral preform was considerably higher than that of the pressure hull because of the infinite principal radius of the meridian of each cone segment. The Huber–von Mises stress for the pressure hull and the slope of this stress for the polyhedral preform decreased from its poles to its equator mainly because of the decrease in curvature from the polar to the equator. A sudden increase in stress occurred at each segment boundary of the polyhedral preform, which can be attributed to the geometric discontinuities of the preform. This

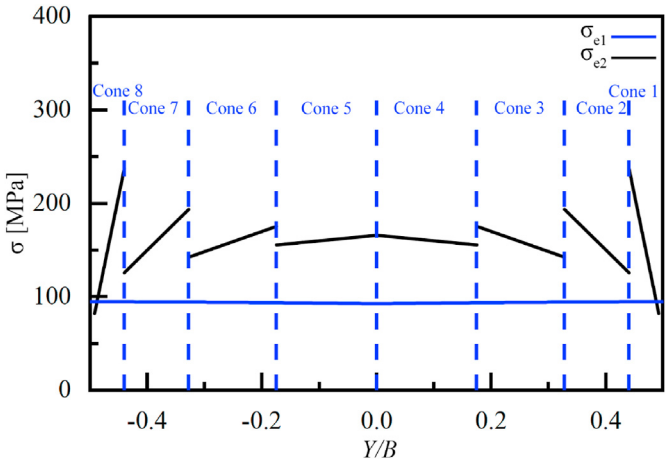

Fig. 3. Huber–von Mises stresses of the longan-shaped pressure hull and longan-shaped polyhedral preform under internal pressure of 1 MPa [analytically obtained using Eqs. (8) and (15), respectively].

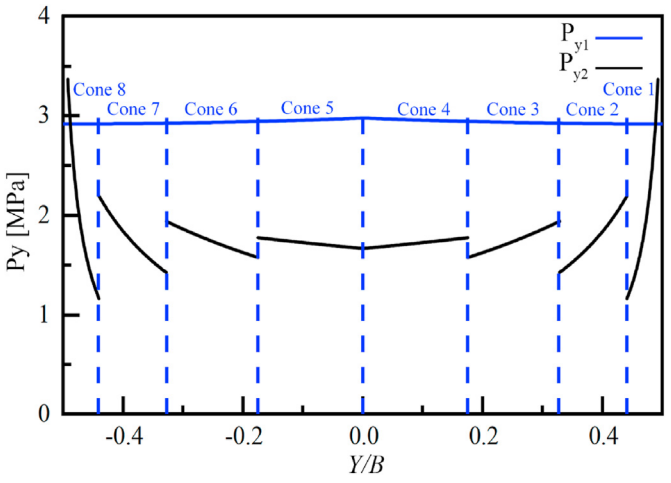

Fig. 4. First yielding loads of the longan-shaped pressure hull and longan-shaped polyhedral preform, analytically obtained using Eqs. (9) and (16), respectively.

phenomenon has also been observed in previous studies related to egg-shaped and toroidal pressure hulls (Zhang et al., 2022a, 2022b, 2022c).

According to Eqs. (9) and (16), the yielding load of the polyhedral preform was lower than that of the pressure hull. Fig. 4 depicts the first yielding loads of the pressure hull and polyhedral preform when Eqs. (9) and (16) were used, respectively. The results indicate that the longan-shaped pressure hull might be obtained through suitable plastic deformation of the materials with an

Table 2
Analytical results obtained for the Huber–von Mises stress of the longan-shaped polyhedral preform by using Eq. (13).

Cones	P_2 [MPa]	t_2 [mm]	α_i [°]	$cos\ \alpha_i$	$X_{2\ min}$ [mm]	$X_{2\ max}$ [mm]	$\sigma_{e2\ min}$ [MPa]	$\sigma_{e2\ max}$ [MPa]
Cone 1	1	1.065	70.25	0.34	34.39	99.25	82.25	237.37
Cone 2	1	1.065	50.35	0.64	99.25	152.58	126.10	193.86
Cone 3	1	1.065	30.21	0.87	152.58	187.82	142.61	175.55
Cone 4	1	1.065	10.04	0.98	187.82	200.00	155.76	165.95
Cone 5	1	1.065	10.04	0.98	187.82	200.00	155.76	165.95
Cone 6	1	1.065	30.21	0.87	152.58	187.82	142.61	175.55
Cone 7	1	1.065	50.35	0.64	99.25	152.58	126.10	193.86
Cone 8	1	1.065	70.25	0.34	34.39	99.25	82.25	237.37

increase in bulging pressure. For the polyhedral preform, the yielding loads of the first and eighth cones were considerably higher than those of the other cones because of the small curvatures at the north and south poles of the preform. This phenomenon indicates that the first and eighth cones of the polyhedral preform undergo plastic deformation with difficulty during dieless bulging. The first yielding loads of the pressure hull exhibited marginal variations and were similar to those of spherical shells. This finding is attributed to the fact that the pressure hull had a small curvature deviation.

3. Experimental methodologies

This section details the methods and equipment used for manufacturing the longan-shaped polyhedral preform, measuring the shape and thickness of the polyhedral preform and longan-shaped pressure hull, performing dieless bulging for the polyhedral preform, and conducting an external hydrostatic test on the pressure hull.

3.1. Manufacturing of the polyhedral preform

The manufacturing of the longan-shaped polyhedral preform involved processes such as numerical blanking, spot welding, assembling, and seam welding. Details of the manufacturing method are depicted in Fig. 5. First, eight fan-shaped plates and one top plate were blanked from a steel sheet with an average measured thickness of 1.065 mm. In addition, for assembling an inlet valve, a hole with the diameter of 20 mm was cut at the centre of the top plate. A base plate with a diameter of 80 mm and a thickness of 20 mm was used to facilitate positioning. The poles of the pressure hulls are probably the manhole or observation window in real underwater conditions (Zhang et al., 2017a). Therefore, the bulging accuracy of the poles of the pressure hull were not concentrated in this study. Blanking was performed using a computer numerical control (CNC) laser blanking machine (CMO2560-B; Han's Yueming Laser Group, China). Second, the fan-shaped plates were cold-bent into cones by using a CNC bending machine (CD-700; Chuangde Machinery Equipment Co., Ltd, China). Third, the cones, inlet valve, and base plate were assembled and spot-welded into a polyhedral preform. Finally, the assembled polyhedral preform was manually welded through tungsten inert gas welding (YC-500WX N-Type, Panasonic, Japan). The pulse current in the manufacturing process was 40 A, and the pulse frequency was 40 Hz.

3.2. Measurements and tests

The experimental procedures performed on the polyhedral preform [Fig. 6(a)–(c)] and pressure hull [Fig. 6(d)–(f)] are depicted in Fig. 6. In Fig. 6, 1 = longan-shaped polyhedral preform, 2 = three-dimensional scanner, 3 = nondestructive thickness measurement device, 4 = digital pressure transducer, 5 = manual pressure pump, 6 = dynamic data collector, 7 = hyperbaric chamber, and 8 = hydraulic lift.

3.2.1. Shape measurement

The external geometries of the polyhedral preform and pressure hull were measured before and after thickness measurement, respectively. An optical three-dimensional scanner (Cronos 3D, Open Technologies, Italy) with an error of less than 0.02 mm was used for shape measurement, and the software program used with

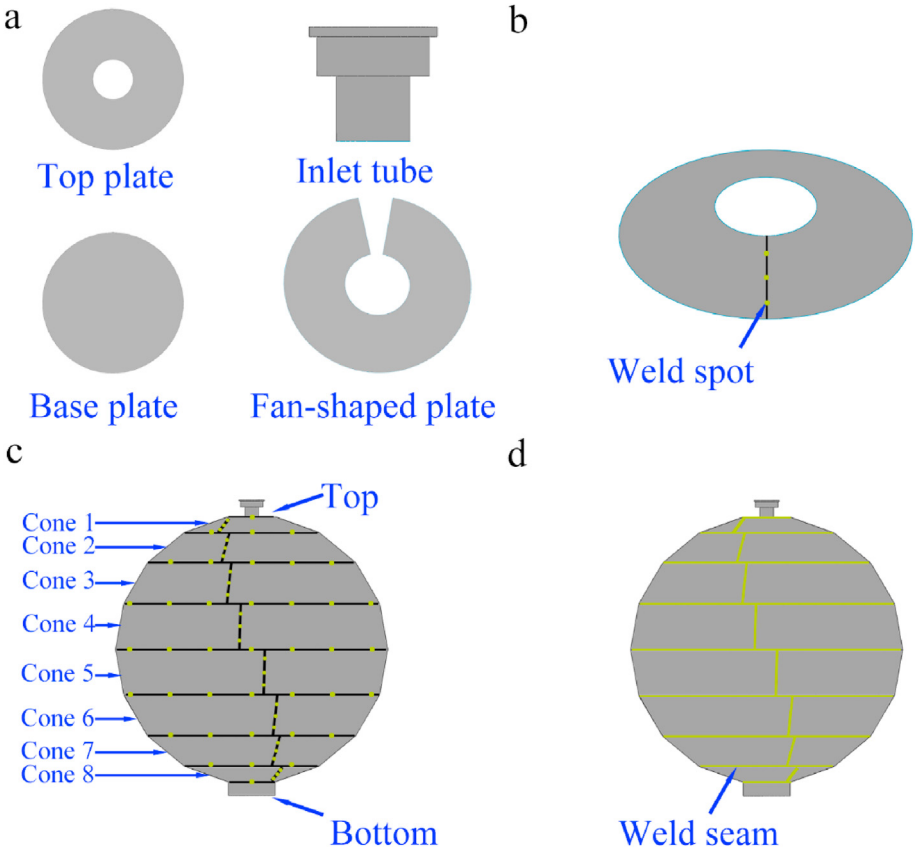

Fig. 5. Manufacturing procedures of the longan-shaped polyhedral preform: a = numerical blanking, b = bending, c = spot welding, and d = seam welding.

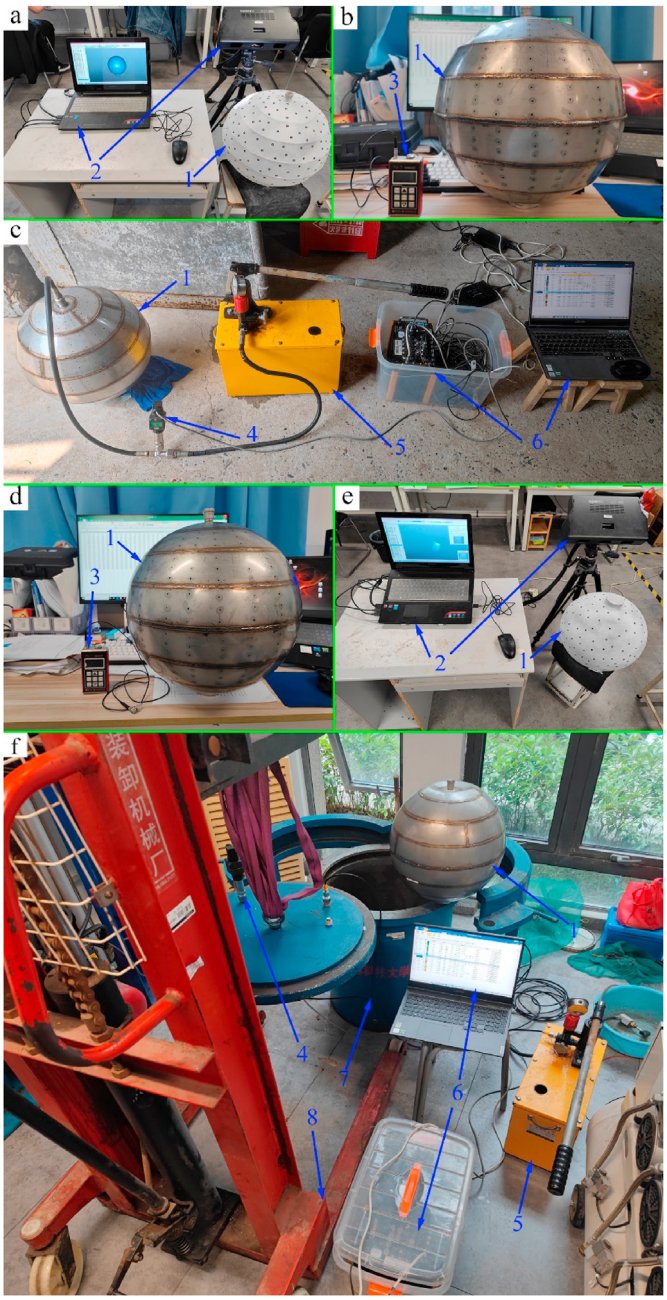

Fig. 6. Experimental procedures conducted on the (a–c) longan-shaped polyhedral preform and (d–f) longan-shaped pressure hull: a = shape measurement, b = thickness measurement, c = dieless bulging, d = thickness measurement, e = shape measurement, and f = buckling test.

this scanner was Optical RevEng. As depicted in Fig. 6(a), a thin layer of contrast enhancement film was sprayed onto the surface of the preform to reduce light refection, and many circular marking stickers were pasted onto the sprayed surface to ensure accurate photo stitching. Optical RevEng was used to generate the computer-aided-drafting geometry of the manufactured polyhedral preform from the optical data. The external geometry of the pressure hull was optically measured after thickness measurement. As depicted in Fig. 6(e), the optical measurement processes used for the pressure hull were the same as those used for the polyhedral preform.

3.2.2. Thickness measurement

The thickness of the polyhedral preform and pressure hull were measured before and after the bulging test, respectively. Thus, the thickness variation during the bulging test could be determined. A nondestructive thickness measurement device (DAKOTA/PX-7; Sonatest Corporation, USA) with an error of less than 0.002 mm and an ultrasonic couplant (Elecall, China). The marking stickers were removed after the scanning process was completed [Fig. 6(a)]. The contrast enhancement film was washed off with ethanol (CH_3CH_2OH, >99.7%). Subsequently, the thickness of the manufactured polyhedral preform was ultrasonically measured using the aforementioned nondestructive thickness measurement device. The transducer of this device was separated from the test object by the couplant. As depicted in Fig. 6(b), a total of 26 measurement points were equally distributed on each meridian of the polyhedral preform, and the meridians were 15° apart from each other; thus, the total number of measurement points was 624 (26 × 24). The thickness of the pressure hull was ultrasonically measured after the bulging test. As depicted in Fig. 6(d), the ultrasonic measurement processes used for the pressure hull were the same as those used for the polyhedral preform.

3.2.3. Bulging test

The bulging test was conducted after measurement of the shape and thickness of the polyhedral preform. The following devices were used in the bulging test: a manual pressure pump (SRB-30X; Zhenhuan Hydraulic Apparatus, China) with a maximum working pressure of 30 MPa and a single stroke having a maximum flow of 38 mL, a digital pressure transducer (SUP−P3000; United Test Automation, China) with an error of less than 0.15 MPa and a maximum recording pressure of 20 MPa, and a data acquisition system (DH5902; Donghua Test Technology, China) with a recording frequency of 50 Hz. As depicted in Fig. 6(c), the polyhedral preform was filled with tap water through the inlet valve. Hydrostatic pressure was internally applied on the polyhedral preform to conduct dieless bulging by using the manual pressure pump, the digital pressure transducer was used to record the applied pressure, and the test data were recoded using the aforementioned data acquisition system.

3.2.4. Buckling test

The buckling test was preformed after the shape and thickness measurement of the bulged preform is finished. After the polyhedral preform was bulged, the longan-shaped pressure hull was obtained. The devices used in the buckling test were a cylindrical steel hyperbaric chamber, a hydraulic lift, a manual pressure pump, a digital pressure transducer, and a data acquisition system. The hydraulic lift was used to move the cover slab of the cylindrical steel hyperbaric chamber located at Jiangsu University of Science and Technology. This chamber has an internal diameter of 500 mm, an internal height of 500 mm, and a wall thickness of 30 mm. These geometrical dimensions resulted in a maximum testing load of 10 MPa. The pressure medium, manual pressure pump, digital pressure transducer, recording frequency, and data acquisition system are the same as those used for the preform. The collapse of the pressure hull was indicated by a loud sound caused by the sudden change in shell geometry. After the pressure hull collapsed, the pressure hull was removed from the hyperbaric chamber.

Notably, an additional load F_R acted at the north pole of the pressure hull during the external hydrostatic test; this load can be attributed to the positive buoyancy of the pressure hull. A sketch of the hyperbaric chamber and the test sample are depicted in Fig. 7. In this figure, 1 = heavy steel plate, 2 = net bag, 3 = longan-shaped pressure hull, 4 = hyperbaric chamber, 5 = locking cover, 6 = cover slab, 7 = intake valve, 8 = digital pressure sensor, and 9 = drainage

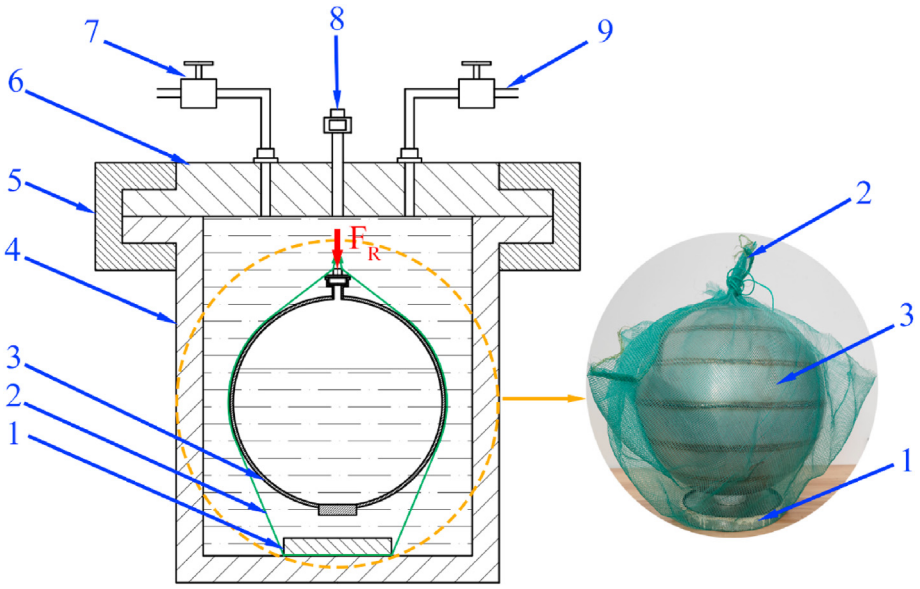

Fig. 7. Sketch of the adopted hyperbaric chamber and the test sample.

valve. Before the hyperbaric test was started, to reduce the effect of positive buoyancy on bucking load, approximately 70% of the pressure hull was filled with water. The pressure hulls used in real-world underwater conditions are designed to have positive buoyancy. For example, underwater observatories are located at a constant depth and anchored to the seabed to against positive buoyancy (Zingoni and Enoma, 2020). The pressure hull and heavy steel plate were wrapped with a net bag to maintain the position of the pressure hull in the hyperbaric chamber and to prevent contact between the pressure hull and the inner surface of the hyperbaric chamber.

4. Results and discussion

This section presents the measured thickness and shape data as well as the results of the bulging and buckling tests. Finite-element models for numerical analysis were developed on the basis of the shape measurement results. The numerical and experimental results were then compared.

4.1. Measurement analysis

4.1.1. Thickness analysis

The measured thicknesses of the polyhedral preform and pressure hull exhibited normal distributions (Fig. 8). The thickness range for the pressure hull was wider than that for the polyhedral preform because of the inconsistent deformation of the preform and the spheroidization principle (Wang et al., 2018). The spheroidization principle means that the larger ones of the first and second principal radius must decrease to reduce the radius of curvature to divide the load, while the smaller ones should become larger to reduce the load. Thus, during deformation, the radii of curvature change continuously throughout the shell until the required uniform radius of the sphere is reached. The thickness of the polyhedral preform was reduced when it bulged because of the constant volume principle (Zhang and Wang, 2015).

The statistical distributions of the measured thicknesses of the polyhedral preform are depicted in Fig. 8(a). The thickness of the polyhedral preform ranged from 1.058 to 1.074 mm. Approximately 95% of the measured thicknesses of the preform were distributed in the range of 1.062−1.068 mm. The mode and average of the measured thicknesses of the preform were 1.064 and 1.065 mm, respectively. The statistical distributions of the measured thicknesses of the pressure hull are displayed in Fig. 8(b). The thickness of the pressure hull ranged from 1.046 to 1.066 mm. Approximately 80% of the measured thicknesses of the pressure hull were distributed in the range of 1.052−1.058 mm. The mode and average

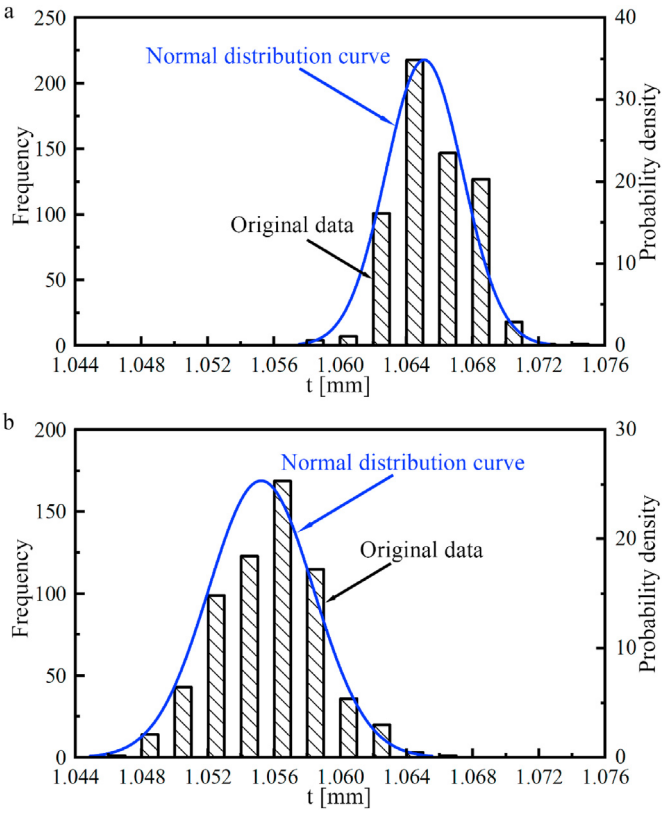

Fig. 8. Statistical distributions of the measured thicknesses of the (a) longan-shaped polyhedral preform and (b) longan-shaped pressure hull.

Table 3
Statistical results of the measured thicknesses of the longan-shaped polyhedral preform and longan-shaped pressure hull.

	T_{max} [mm]	T_{min} [mm]	T_{ave} [mm]	*St. dev*
Preform	1.074	1.058	1.065	0.002
Bulged	1.066	1.046	1.055	0.003

of the measured thicknesses of the pressure hull were 1.056 and 1.055 mm, respectively.

The standard deviation of the thickness of the polyhedral preform and pressure hull were only 0.002 and 0.003, respectively. Thus, the thickness distribution of the polyhedral preform was more concentrated than that of the pressure hull. The statistical results of the measured thicknesses of the polyhedral preform and pressure hull are listed in Table 3, and the thickness contours of these parts are depicted in Fig. 9. As displayed in Fig. 9, the thickness distributions of the polyhedral preform and pressure hull were uniform.

The measured thickness contours of the polyhedral preform are depicted in Fig. 9(a). The wall thickness of the polyhedral preform exhibited marginal changes at each cone boundary, and minor variations were observed in the circumferential direction in most situations. The sudden change in the wall thickness in the circumferential direction is attributed to the longitudinal weld seams. The measured thickness contours of the pressure hull are displayed in Fig. 9(b). Of the eight cones, cones 4 and 8 exhibited the smallest wall thicknesses. More than 50% of cone 4 and 70% of cone 8 had a wall thickness of less than 1.053 mm. The remaining area of the cones are ranged from 1.057 to 1.064 mm.

4.1.2. Shape analysis

To facilitate the comparison between the geometric shape of the manufactured shells and the nominal ones, the inlet valve, top plate and base plate were ignored using the Geomagic Studio preprocessing software program. GOM Inspect was used for analysing the shape measurements. A positive geometric deviation indicated that the measured geometry had a larger bulge than did the nominal geometry. By contrast, a negative geometric deviation indicated that the measured geometry had a smaller bulge than did the nominal geometry. As depicted in Fig. 10, the geometric deviations of the polyhedral preform and pressure hull were reasonable. The geometric deviations of the polyhedral preform followed a nearly normal distribution, which was wider than the distribution of the geometric deviations of the pressure hull. The geometric accuracy of the pressure hull was higher than that of the polyhedral preform because of the spheroidization pressurising process in the bulging test (Wang et al., 2018). Almost all the

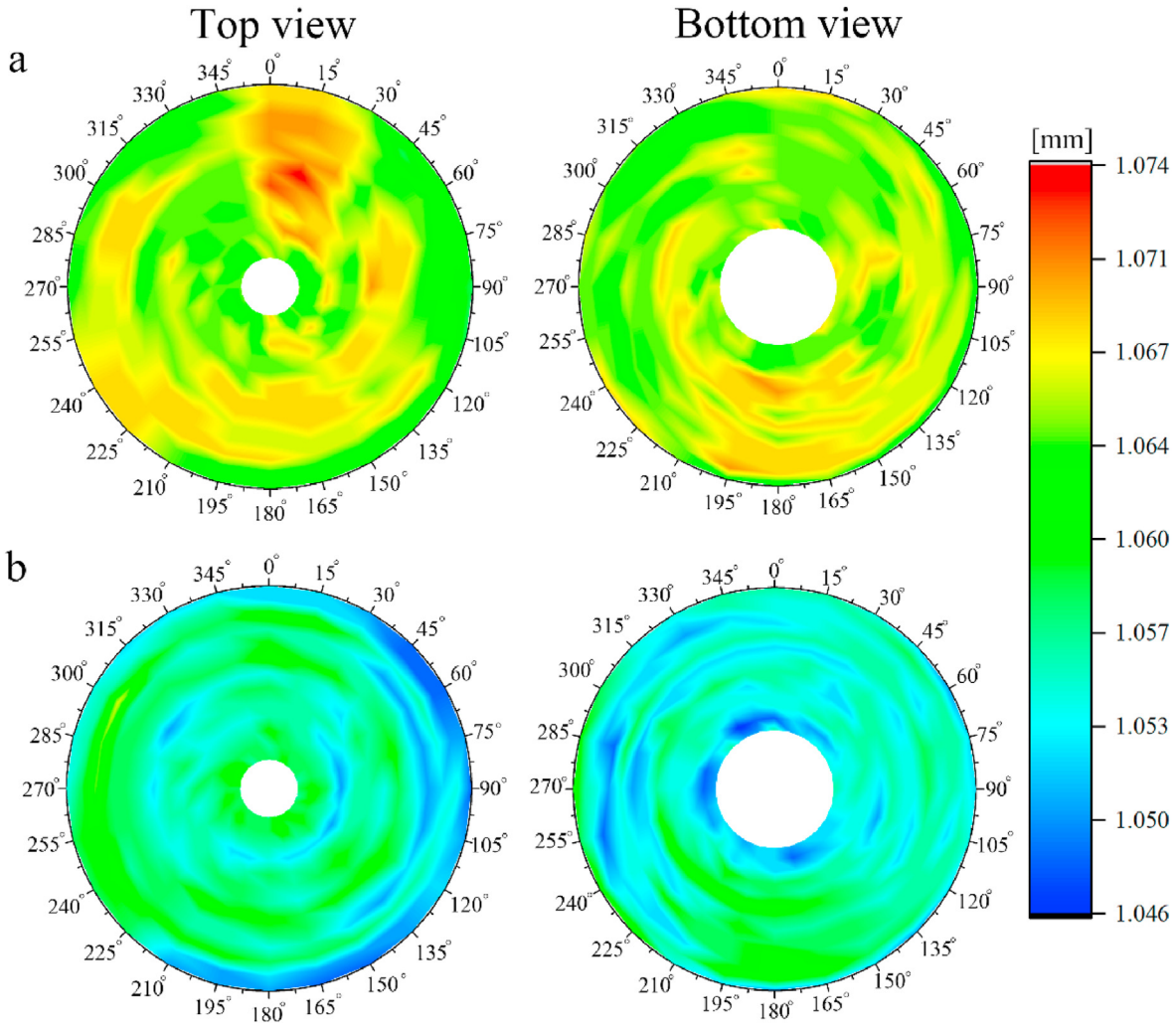

Fig. 9. Measured thickness contours of the (a) longan-shaped polyhedral preform and (b) longan-shaped pressure hull.

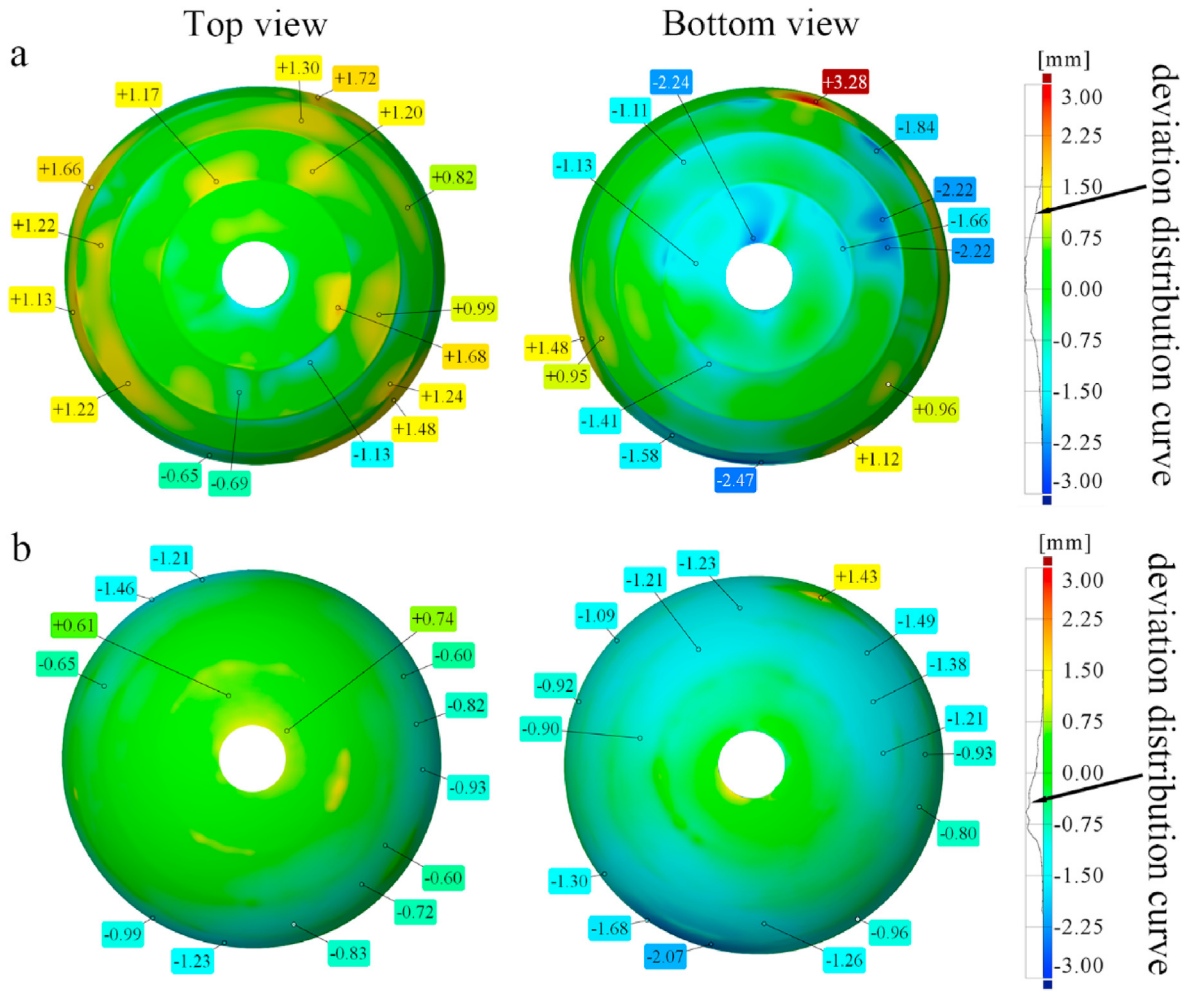

Fig. 10. Measured geometries of the longan-shaped (a) polyhedral preform and (b) pressure hull. The legends and contours indicate the deviations of the measured geometries from the nominal geometry (Fig. 1).

deviations of the polyhedral preform in the top view had positive values. By contrast, almost all the deviations of the preform in the bottom view had negative values. Moreover, the geometric deviations of the pressure hull in the bottom view were considerably smaller than those in the top view.

The measured geometry of the polyhedral preform is depicted in Fig. 10(a). The maximum geometric deviation of the preform was 3.28 mm, which is 1.91% of the circumferential radius of the pressure hull; this deviation is attributed to the CNC bending process. The majority of the remaining geometric deviations occurred near the weld seams and were in the range of −0.75 to 0.75 mm.

The measured geometry of the pressure hull is displayed in Fig. 10(b). The large geometric deviations in the top view occurred in the welding area. These deviations are attributed to the fact that the nominal geometry shown in Fig. 1 excluded the weld seams. The maximum positive geometric deviation in the bottom view was 1.43 mm, which corresponded to the position of maximum deviation on the polyhedral preform. Most of the geometric deviations of the pressure hull were in the range of −1.00 to 0.75 mm. Considering that the major axis of the nominal geometry (Fig. 1) has a length of 400 mm, the aforementioned deviations are reasonable.

4.2. Bulging analysis

4.2.1. Experimental analysis

The final bulging pressure applied to the polyhedral preform was 3.62 MPa, which was the maximum internal pressure capacity of the internal pressure hull. The dieless bulging of the pressure hull under various internal loads is depicted in Fig. 11, and the corresponding load values are shown in Fig. 12. The polyhedral preform did not exhibit notable shape changes when the bulging pressure was 0−1 MPa. This phenomenon agreed well with the analytical results for the first yielding loads of the polyhedral preform (Fig. 4) because the minimum first yielding load of the preform was 1.2 MPa. The first deformation occurred on the top plate when the bulging pressure was 1.5 MPa. This phenomenon also agreed well with the analytical results for the first yielding load of the polyhedral preform because the first yielding loads of the first and eighth cones were less than 1.5 MPa. The polyhedral preform bulged slightly when the bulging pressure was 2 MPa because the first yielding load of the preform was less than 2 MPa at all points except for some parts of the first and eighth cones. The dividing lines between the cones completely disappeared when the bulging

Fig. 11. Dieless bulging of the longan-shaped pressure hull under various internal loads.

pressure was 2.5 MPa because most of the first yielding loads of the preform were less than 2.5 MPa. Subsequently, a smooth geometry was obtained when the bulging pressure exceeded 3 MPa because most of the preform was fully plastically deformed at this pressure level. At a final bulging pressure of 3.62 MPa, a sound longan-shaped pressure hull was obtained.

The pressurising process in the bulging test involved three stages, with linear deformation characteristic being observed in the first and third stage, and nonlinear deformation characteristic being observed in the second stage. The pressure–time curve recorded in the dieless bulging test conducted on the pressure hull is depicted in Fig. 12. The pressurising process required approximately 220 s. The first stage of pressurisation occurred between points A1 and A3 in the graph displayed in Fig. 12. The polyhedral preform did not exhibit notable shape changes in the first stage, because the first stage was with the linear elastic deformation characteristic, and the pressure in this stage were below the analytical result of first yielding load. The second stage occurred between points A3 and A6. The nonlinearities recorded in this stage could be the plastic flow of the material just after exceeding the yield point. The third stage occurred between points A6 and A8 and was the last stage in the bulging test. The nearly linear deformation

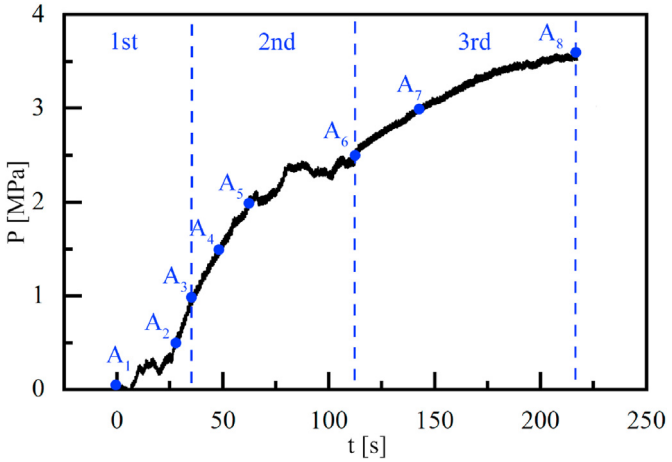

Fig. 12. Pressure–time curves recorded in the dieless bulging test conducted on the longan-shaped pressure hull.

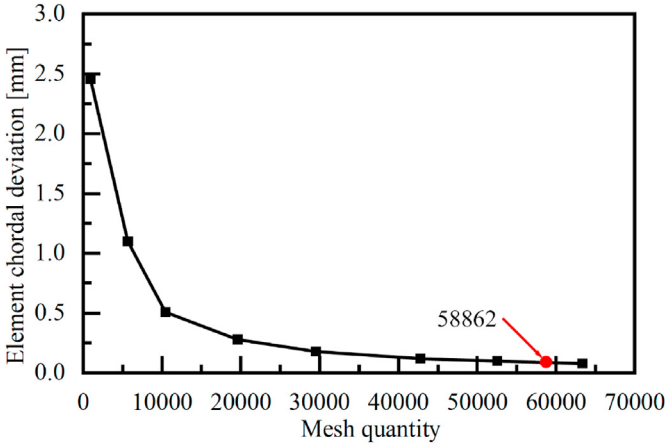

Fig. 14. Mesh convergence study of the FEM model for the bulging analysis.

characteristic was observed in the third stage. Because the shell was in full plastic deformation, the pressure in this stage had been exceeded nearly all yield pressure of the preform. The pressure–time curve exhibited nonlinear monotonous increments at this stage. The minimum pressurisation rate in the bulging test occurred in the third stage, which allowed the final bulging pressure to be controlled.

4.2.2. Numerical analysis

For further studying the bulging of the polyhedral preform, general static analysis was conducted using the finite element method (FEM), which can be applied in ABAQUS. The painted polyhedral preform and the numerical model of the bulging of the preform are depicted in Fig. 13. For simplifying the numerical analysis, the inlet valve was excluded, and the hole on the top plate was filled (the plate had a thickness of 1.065 mm). The numerical model of the polyhedral preform was meshed using linear reduced-integration quadrilateral (S4R) elements. According to the mesh convergence study which depicted in Fig. 14, the preform comprised 58,862 elements. To prevent rigid body motion, the boundary of the base plate was fixed, with $U1 = U2 = U3 = UR1 = UR2 = UR3 = 0$. In ABAQUS, the degrees of freedom 1, 2 and 3 represent the displacement of x, y and z axes, respectively. The degrees of freedom 4, 5 and 6 represent the rotation of x, y and z axes, respectively. Where $U1 = U2 = U3 = 0$ indicated that all nodes we selected were restricted in degrees of freedom 1, 2 and 3, respectively. $UR1 = UR2 = UR3 = 0$ indicated that all nodes we selected were restricted in degrees of freedom 4, 5 and 6, respectively.

The material properties used in the numerical analysis are listed in Fig. 2.

Attention should be paid that the welding residual stress were not considered in the FE analyses, because the welding residual stress can be significantly eliminated with the development of plastic deformation during the bulging process, which has been experimentally proved by the previous researches (Yuan et al., 1996).

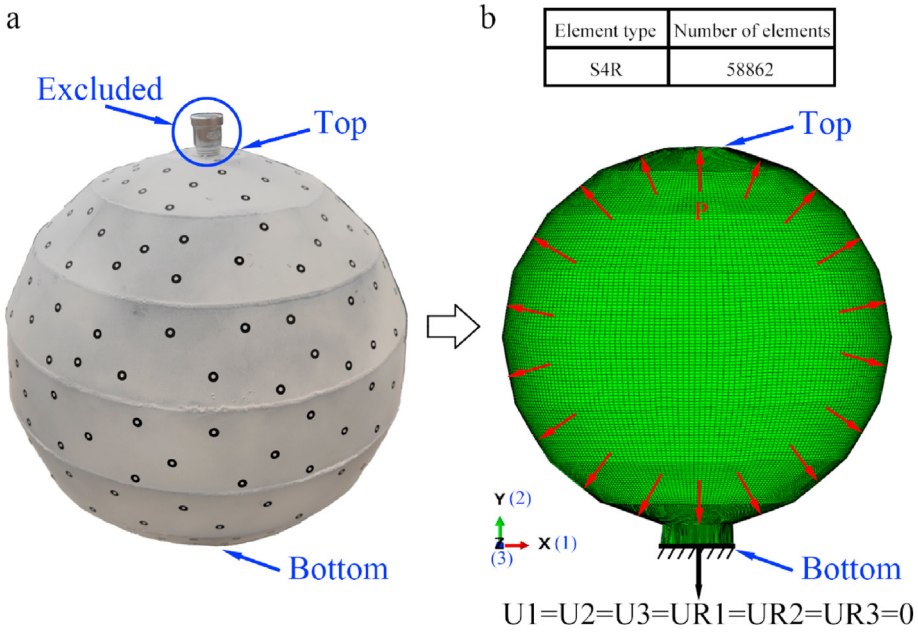

Fig. 13. (a) Painted preform and (b) numerical model for the bulging of the longan-shaped polyhedral preform.

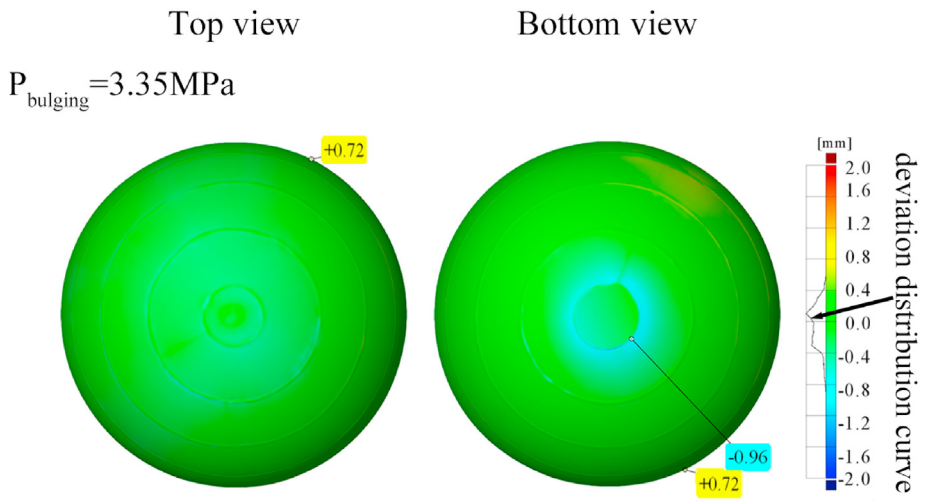

Fig. 15. Numerical and experimental longan-shaped pressure hulls obtained under dieless bulging pressure (P) of 3.35 MPa.

Two processes were simulated in the numerical analysis of the bulging of the preform: internal pressure loading and springback. As depicted in Fig. 13, these processes were examined through general nonlinear static analysis. The maximum increment, minimum increment, initial increment, and maximum number of increments in the process were 0.02, 10^{-50}, 0.02, and 100, respectively.

On the basis of trial and error, $P = 3.35$ MPa was the most suitable bulging pressure for numerically obtaining a satisfactory pressure hull geometry. The aim we use different bulging load was to obtain the similar geometric shape from numerical analysis and experimental result. Based on the same geometric shape, we can compare the difference of the buckling load and post buckling behavior between numerical analysis and experimental result. The deviation between the numerical and experimental bulging pressure values was 8.1%. The numerical and experimental shapes of the pressure hull under bulging pressure of 3.35 MPa are depicted in Fig. 15. A positive (negative) deviation indicated that the numerical shape had a larger (smaller) bulge than did the experimental shape. The maximum and minimum deviations were 0.72 and −0.96 mm, respectively. Deviation mainly occurred at the boundary of the base plate, which can be attributed to the boundary condition of the numerical analysis. Most of the deviations between the numerical and experimental shapes of the pressure hull were in the range of −0.4 to 0.4 mm.

The numerical thickness results were in good agreement with the experimental thickness results. The deviation between these results can be attributed to the assumption of uniform thickness and the ignoring of the weld seams in the numerical analysis. The numerical and experimental thicknesses of the longan-shaped pressure hull after dieless bulging are displayed in Fig. 16. The numerical thicknesses were obtained along three equidistant meridians under a bulging pressure of 3.35 MPa. Overall, the experimental thickness of the pressure hull was higher than its numerical thickness. The maximum deviation between the numerical and experimental thicknesses was 0.011 mm, which was 0.1% of the average thickness of the experimental result of the pressure hull. The average deviation between these thicknesses was 0.005 mm, which was 0.05% of the average thickness of the experimental result of the pressure hull. The minimum deviation was 7×10^{-7} mm, which indicated that the thicknesses at the two points on the eighth cone were almost the same. In each cone, the

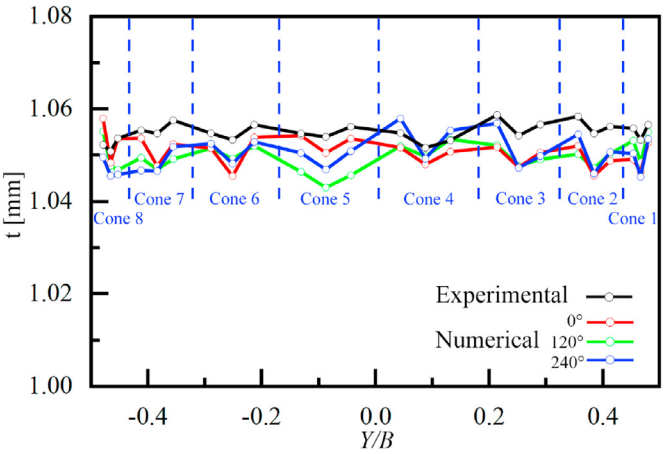

Fig. 16. Numerical and experimental thicknesses of the longan-shaped pressure hull after dieless bulging. Numerical thicknesses were obtained along three equidistant meridians under a bulging pressure of 3.35 MPa.

experimental and numerical thicknesses at the middle point were smaller than those at the other two points because of the boundary effect.

The residual stress of the bulged pressure hull was concentrated in the weld seams and increased from the middle of the cones to the weld seams. By contrast, the plastic strain of the bulged pressure hull was concentrated in the cones and decreased from the middle of the cones to the weld seams. The middle areas of the cones had a lower residual stress and higher plastic strain than did the other areas of the pressure hull because the maximum displacement and deformation occurred in the middle areas of the cones during the bulging test. All the negative plastic strain occurred at the latitudinal weld seams. The aforementioned phenomena have also been observed in previous studies (X. Liu et al., 2022; Zhang et al., 2022b). The residual stress and plastic strain contours of the pressure hull that were obtained through numerical bulging analysis for a bulging pressure of 3.35 MPa are depicted in Fig. 17.

The residual stress contours of the pressure hull that were obtained through numerical bulging analysis are displayed in Fig. 17(a). The residual stress was concentrated at the welding

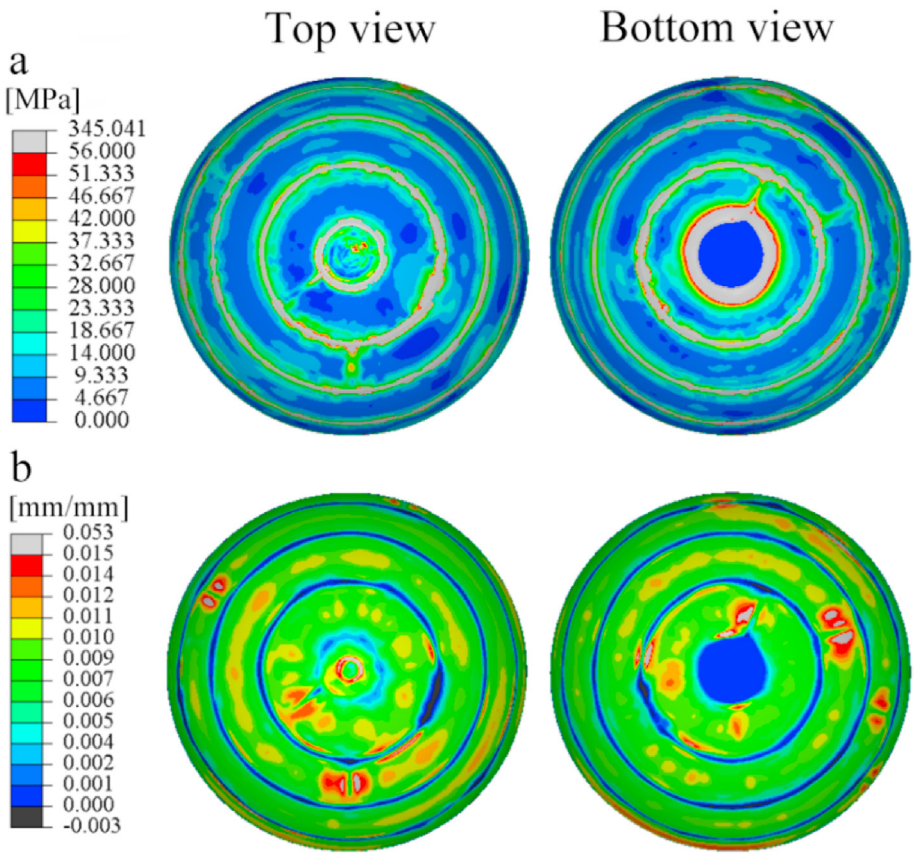

Fig. 17. (a) Residual stress and (b) plastic strain contours of the pressure hull that were obtained through numerical bulging analysis under a bulging pressure of 3.35 MPa.

seams because of the geometric discontinuities of the polyhedral preform. In each cone of the pressure hull, the residual stress in the middle area was considerably lower than that close to the boundary of the weld seams because the deformation was larger in the middle area during the bulging test. The grey zone was considerably larger than other weld seams at the boundary of the base plate, which can be attributed to the boundary condition of the numerical analysis. Overall, except at the top and base plates, the magnitude and distribution of the residual stress were almost the same in each cone of the pressure hull.

The numerical plastic strain contours of the pressure hull are illustrated in Fig. 17(b). The plastic strain was concentrated in the middle area of each cone because the deformation in this area was greater than that in other areas of the pressure hull during the bulging test. The maximum plastic strain occurred at the boundary of the longitudinal weld seams because of the spheroidization principle (Wang et al., 2018) and because the geometric deviations around the longitudinal weld seams were larger than those in other areas of the pressure hull. The plastic strain at the latitudinal weld seams was considerably lower than that in the other areas of the pressure hull, and all the negative plastic strain occurred at the latitudinal weld seams because of the deformation of the cones near these seams.

4.3. Buckling analysis

4.3.1. Experimental analysis

The pressure history exhibited a nearly bilinear character in the prebuckling stage, and the pressure then decreased suddenly after the pressure hull collapsed. The hydrostatic test involved three stages and lasted for approximately 120 s. The final collapse load for the pressure hull (P_{cr}) was 1.684 MPa. The pressure–time curve recorded for the pressure hull in the hydrostatic test is presented in Fig. 18. The first stage of the hydrostatic test was the preparation stage. This stage lasted for 34 s, and the loading rate in the stage was approximately 0.007 MPa/s. The second stage was the formal testing stage. This stage lasted for 64 s, and the loading rate in the stage was 0.021 MPa/s. To increase the loading rate, the pumping operation was conducted rapidly in the second stage. In the third stage, a sudden jump occurred in the pressure–time curve at approximately 102 s, and the load corresponding to this time

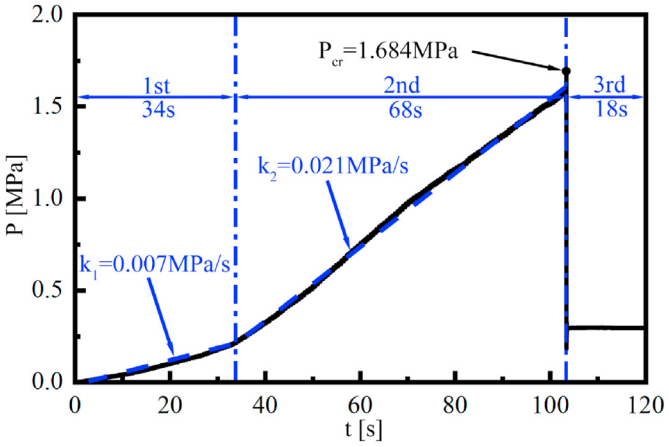

Fig. 18. Pressure–time curve obtained in the hydrostatic test for the longan-shaped pressure hull. The peak point corresponds to the collapse load.

(1.684 MPa) was considered the collapse load.

In the collapse mode of the pressure hull, it exhibited an oblate ellipsoidal local dent at its north pole. Such a collapse mode is typical of shells of revolution that are subjected to uniform external pressure, and this was observed in a study of Cassini oval shells by Zhang et al. (2018b). Photographs of the pressure hull before and after an external pressure test are depicted in Fig. 19. The aforementioned collapse mode occurred because of the following reasons. First, to achieve consistency with practical working conditions for a longan-shaped pressure hull (Zingoni and Enoma, 2020), the experimental simulated the anchoring state of the pressure hull; thus, an additional concentrated force was applied at the north pole of the pressure hull. Second, the inlet valve at the north pole caused stiffness variation and the boundary effect. Third, the north pole was the most difficult location to bulge because of the stiffness improvement caused by the inlet valve. Therefore, the north pole exhibited the minimum deformation and lower material hardening than did other locations after the bulging test.

4.3.2. Numerical buckling analysis

For further investigating the buckling behaviour of the pressure hull, general static analysis and nonlinear arc length analysis were conducted using the FEM in ABAQUS. The numerical model for the buckling of the pressure hull is depicted in Fig. 20. The mesh convergency study of the FEM model for buckling analysis is depicted in Fig. 21. The preprocessing method adopted for the pressure hull was almost the same as that adopted for the polyhedral preform. The hole at the north pole of the pressure hull was filled (the plate has a thickness of 3 mm); the inlet valve increased the stiffness in this area. The element type, material properties, and boundary conditions adopted for the numerical analysis of the pressure hull were the same as those adopted for the numerical analysis of the polyhedral preform. The total number of elements used to model the pressure hull was 46,002.

Two steps were involved in the buckling analysis of the pressure hull. As depicted in Fig. 20, the first step involved conducting nonlinear general static analysis by considering the influence of positive buoyancy on the buckling behavior of the pressure hull. The parameters used in this analysis for the pressure hull were the same as those used for the analysis of the polyhedral preform. The load used in the first step was the concentrated force applied on four nodes of one element in the middle of the north pole of the

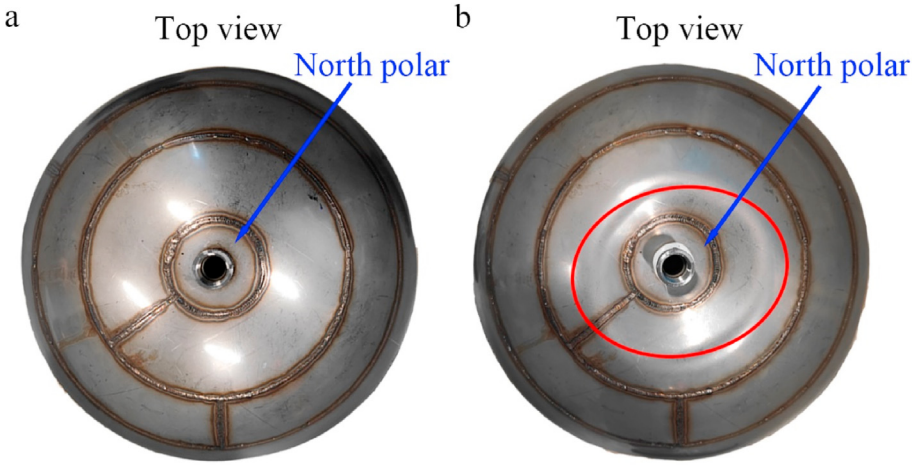

Fig. 19. Photographs of the longan-shaped pressure hull (a) before and (b) after an external pressure test.

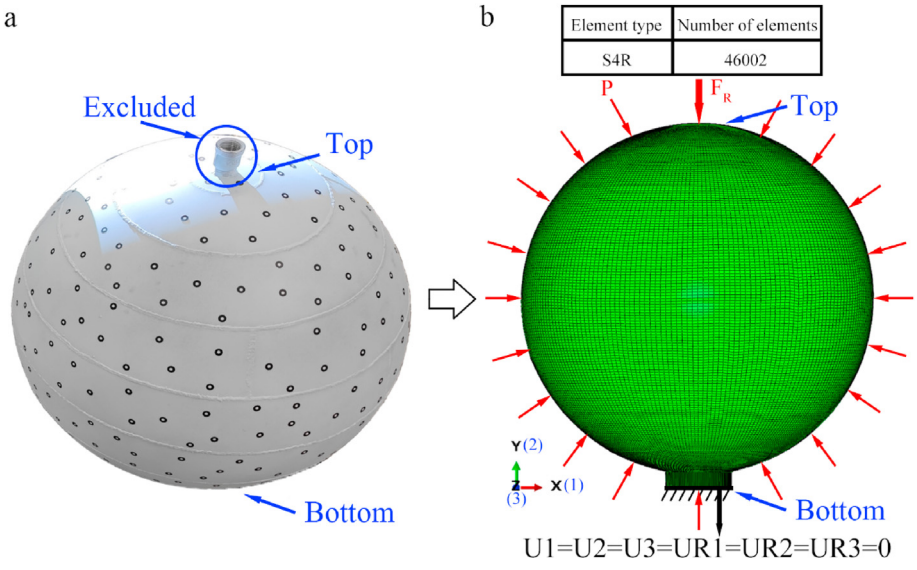

Fig. 20. (a) Bulged pressure hull and (b) numerical model for the buckling of the longan-shaped pressure hull.

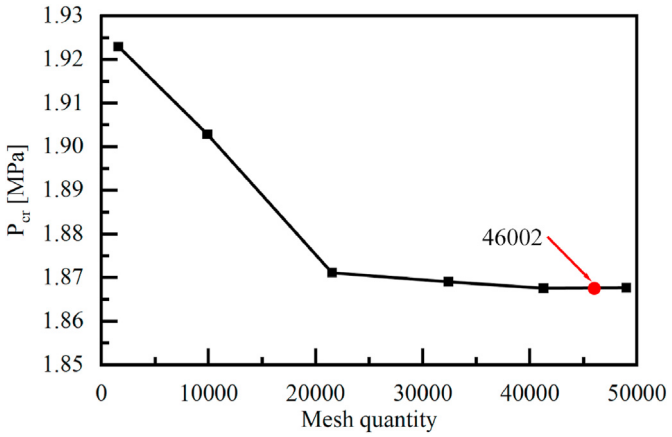

Fig. 21. Mesh convergence study of the FEM model for the buckling analysis.

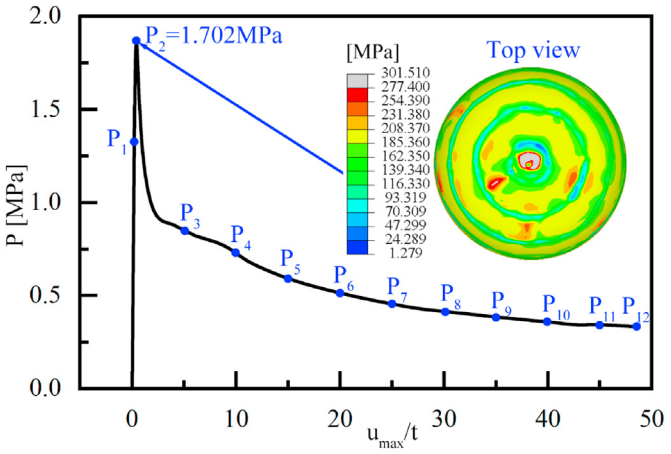

Fig. 22. Pressure–deformation curves obtained through the numerical buckling analysis of the longan-shaped pressure hull when 70% of the pressure hull was filled with water.

pressure hull to simulate the additional load caused by positive buoyancy. The second step involved the application of external pressure by using the static Riks method. The Riks method uses the load magnitude as an additional unknown, it solves simultaneously for loads and displacements. Therefore, another quantity must be used to measure the progress of the solution, ABAQUS/Standard uses the "arc length", along the static equilibrium path in load-displacement space. This approach provides solutions regardless of whether the response is stable or unstable. The maximum arc length increment, minimum arc length increment, initial arc length increment, and total arc length scale factor associated with the second step were 0.02, 10^{-50}, 0.02, and 1, respectively. The load used in the second step was a unit reference pressure that was applied on the external surface of the pressure hull.

The pressure hull exhibited a nonlinear buckling mode. The numerical buckling loads of the pressure hull under various positive buoyancy values are listed in Table 4. By measuring the weight of the empty shell and the shell injected water, we can know the weight of the injected water. Comparing the volume of the injected water with the inner volume of the shell we measured by CAD software NX, we can control and measure the water injection ratio. The numerical linear buckling loads of the pressure hull were considerably higher than its numerical nonlinear buckling loads. The numerical nonlinear buckling loads were closer to the experimental buckling loads than were the numerical linear buckling loads, which indicated that the pressure hull had a nonlinear buckling mode. As the water injection ratio was increased, the positive buoyancy decreased, and the nonlinear bucking load increased. The linear bucking load decreased with an increase in the water injection ratio. Positive buoyancy was reduced into 7.9 N when the water injection ratio was 80%. No buoyancy was applied to the pressure hull if the water injection ratio was 90%–100%. We filled almost 70% of the pressure hull with water to simulate practical working conditions. The positive buoyancy was calculated as follows:

$$F_R = V_d \bullet \rho_w \bullet g - M_h \bullet g - W \bullet V_i \bullet \rho_w \bullet g \tag{18}$$

where F_R is the positive buoyancy, V_d is the displacement volume of the pressure hull (33.032 dm^3), ρ_w is the density of water (1 kg/dm^3), g is the gravitational acceleration (9.8 N/kg), M_h is the mass of the pressure hull (6.2 kg), W is the water injection ratio, and V_i is the inner volume of the pressure hull (32.532 dm^3).

The bucking load obtained in the hydrostatic test was 1.684 MPa, and the numerical nonlinear buckling load was 1.702 MPa when the water injection ratio was 70%. The deviation between the experimental collapse load and the numerical buckling load was 1.1%, which indicated that numerical analysis provided an accurate prediction of the buckling load of the pressure hull. The pressure hull lost stability in the plastic deformation range. The pressure–deformation curves obtained through the numerical buckling analysis and the stress contour when the pressure hull was lost stability are depicted in Fig. 22. The stress at the centre of the north pole of the pressure hull was exceeded the yield stress ($\sigma_y = 277.4$ MPa) of the material when the pressure hull lost stability, which can be seen as the grey zone in the stress contour depicted in Fig. 22, it is indicated that the pressure hull lost stability in the plastic deformation range. These curves indicated unstable postbuckling behaviour by the pressure hull. The applied pressure was increased linearly and rapidly until the buckling point, and the buckling load (P_2) was 1.702 MPa. After buckling, the pressure load was rapidly reduced from P_2 to P_3, which indicated that the pressure hull underwent bifurcation buckling. After a pressure load of P_3 was reached, the reduction rate of the pressure load decreased progressively until the end of the numerical analysis.

The numerical buckling mode of the pressure hull involved the formation of an oblate ellipsoidal local dent at the pressure hull's north pole. Fig. 23 displays the deformation changes obtained through the numerical buckling analysis of the pressure hull under a water injection ratio of 70%. A small dent was formed at the north pole of the pressure hull when the pressure load reached the first yielding point (P_1), and buckling occurred at this location when the

Table 4
Numerical buckling loads of the longan-shaped pressure hull under various positive buoyancy values.

Water injection ratio	Positive buoyancy [N]	Buckling load [MPa]	
		Nonlinear	Linear
0%	262.954	0.578	4.950
10%	231.072	0.739	5.064
20%	199.191	0.901	5.061
30%	167.310	1.064	5.058
40%	135.428	1.227	5.055
50%	103.547	1.452	5.052
60%	71.665	1.547	5.051
70%	39.784	1.702	5.046
80%	7.903	1.853	5.043
90%	−23.979	N/A	N/A
100%	−55.860	N/A	N/A

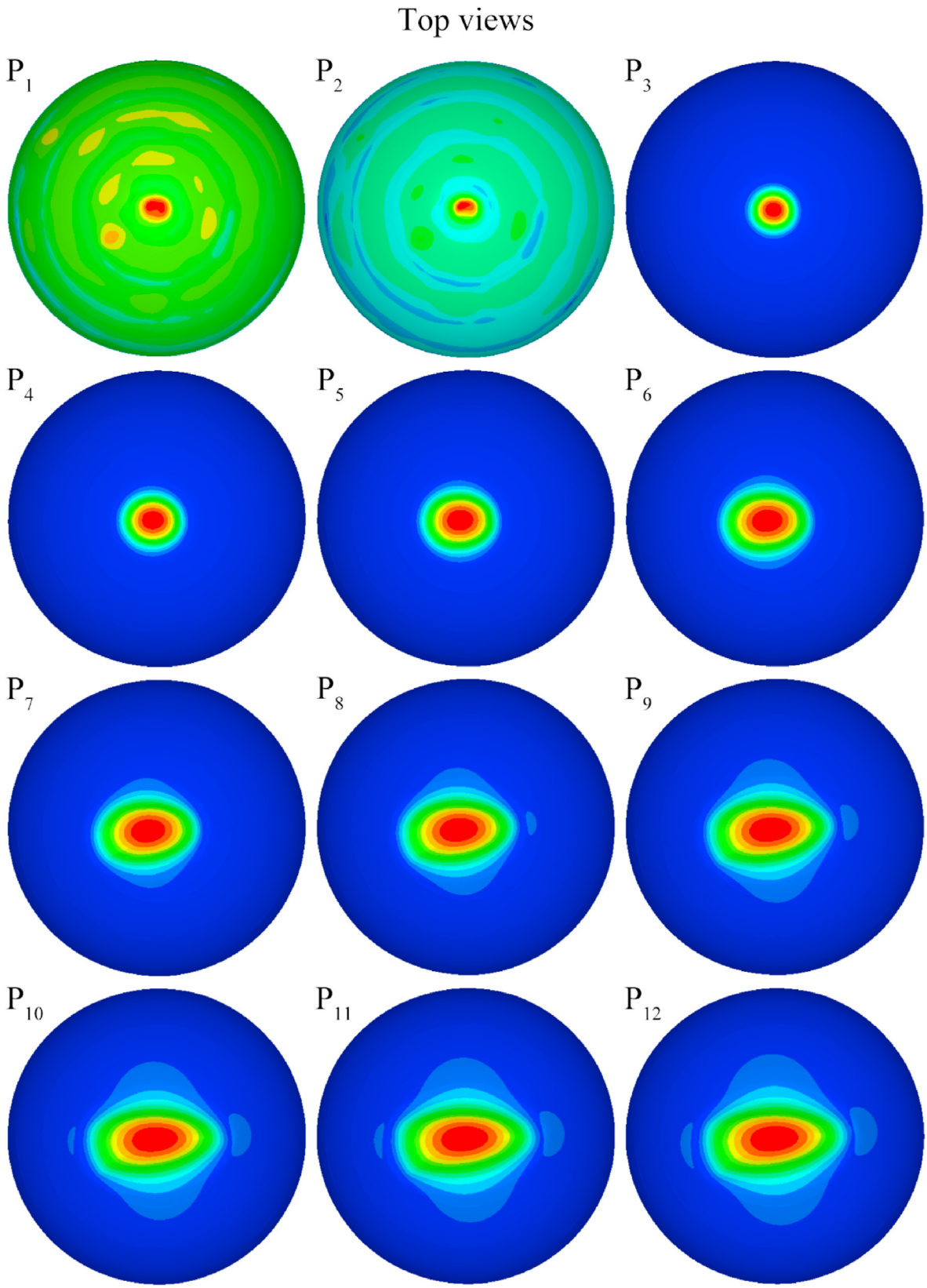

Fig. 23. Deformation changes obtained through the numerical buckling analysis of the pressure hull under a water injection ratio of 70%. All symbols in this figure are as marked in Fig. 22.

pressure load reached the buckling point (i.e., $P_2 = 1.702$ MPa). With an increase in the displacement of the dent, it developed into a large oblate ellipsoid, which is highly consistent with the experimental results depicted in Fig. 19.

5. Conclusions

In this study, the dieless bulging of a longan-shaped polyhedral preform was analytically, numerically, and experimentally investigated. Moreover, the buckling of a longan-shaped pressure hull was numerically and experimentally examined. The conclusions of this study are as follows:

(1) The longan-shaped polyhedral preform and longan-shaped pressure hull exhibited symmetric distributions of Huber–von Mises stress and first yielding load. The Huber–von Mises stress of the pressure hull decreased from its poles to its equator. The Huber–von Mises stress of the preform was higher than that of the pressure hull. Conversely, the first yielding load of the preform was smaller than that of the pressure hull. Thus, a longan-shaped pressure hull can be obtained through suitable plastic deformation of a longan-shaped polyhedral preform with an increase in bulging pressure.
(2) The analytical results agreed well with the results of a bulging test, which validated the adopted theoretical methodology and several basic assumptions made during the construction of the analytical model. Thus, analytical analysis is a reliable method for investigating the bulging of a longan-shaped polyhedral preform.
(3) The final bulging pressure applied on the polyhedral preform was 3.62 MPa, which was equal to the internal pressure capacity of the internal pressure hull. The geometry of the pressure hull was accurately measured in the bulging test. The deviations between the measured and nominal geometries of the preform exhibited a normal distribution, and almost all the geometric deviations of the preform in the top view were positive. By contrast, almost all the geometric deviations of the preform in the bottom view were negative. Moreover, the geometric deviations of the pressure hull in the bottom view were considerably smaller than those in the top view.
(4) In numerical bulging analysis, the residual stress of the pressure hull was concentrated at the weld seams, and all negative plastic strain occurred at these seams. These findings indicate that the weld seams of a longan-shaped pressure hull must be subjected to a stress relief process before the practical implementation of the hull.
(5) The buckling load of the pressure hull was 1.684 MPa. The results of a nonlinear numerical analysis agreed well with the results obtained in a buckling test. The pressure hull exhibited a collapse mode typical of shells of revolution that are subjected to external pressure, and the pressure hull was confirmed to buckle in a nonlinear manner. The aforementioned results indicate that numerical analysis is a reliable method for predicting the collapse mode and buckling load of a longan-shaped pressure hull.

To our knowledge, this study is the first to use dieless bulging technology to manufacture a longan-shaped pressure hull and examine its buckling behaviour under external pressure. This technology is effective, economic, and flexible, and it can be used to manufacture not only used atypical internal pressure hulls but also atypical external pressure hulls.

Declaration of competing interest

The authors declare that they have no known competing financial interests or personal relationships that could have appeared to influence the work reported in this paper.

Acknowledgement

This research was supported by the National Natural Science Foundation of China, China (grant number: 52071160).

References

Arbocz, J., Starnes, J.H., 2002. Future directions and challenges in shell stability analysis. Thin-Walled Struct. 40. https://doi.org/10.1016/S0263-8231(02)00024-1.
Błachut, J., 2015. Buckling of cylinders with imperfect length. Journal of Pressure Vessel Technology, Transactions of the ASME 137. https://doi.org/10.1115/1.4027246.
Błachut, J., 2014. Experimental perspective on the buckling of pressure vessel components. Appl. Mech. Rev. 66. https://doi.org/10.1115/1.4026067.
Błachut, J., 2013. Combined stability of geometrically imperfect conical shells. Thin-Walled Struct. 67. https://doi.org/10.1016/j.tws.2013.02.007.
Błachut, J., 2011. On elastic-plastic buckling of cones. Thin-Walled Struct. 49. https://doi.org/10.1016/j.tws.2010.08.005.
Błachut, J., 2010. Developments in strength and stability of shell components used in submersibles. In: Shell Structures: Theory and Applications - Proceedings of the 9th SSTA Conference. https://doi.org/10.1201/9780203859766.ch1.
CCS, 2014. Rules for Construction and Classification of Diving Systems and Submersibles, vol. 5. China Classification Society.
Cerik, B.C., Shin, H.-K., Cho, S.-R., 2013. Probabilistic ultimate strength analysis of submarine pressure hulls. Int. J. Nav. Archit. Ocean Eng. 5. https://doi.org/10.2478/ijnaoe-2013-0120.
Cui, W., 2013. Development of the Jiaolong deep manned submersible. Mar. Technol. Soc. J. 47. https://doi.org/10.4031/MTSJ.47.3.2.
Cui, W., Hu, Y., Guo, W., Pan, B., Wang, F., 2014. A preliminary design of a movable laboratory for hadal trenches. Methods in Oceanography 9. https://doi.org/10.1016/j.mio.2014.07.002.
Enoma, N., Zingoni, A., 2020. Analytical formulation and numerical modelling for multi-shell toroidal pressure vessels. Comput. Struct. 232. https://doi.org/10.1016/j.compstruc.2017.07.013.
Fu, X., Mei, Z., Wang, S., Bai, X., Zhang, E., Chen, G., Li, H., 2023. Design method of combined stiffened pressure hulls with variable-curvature characteristic. Ocean Eng. 281. https://doi.org/10.1016/j.oceaneng.2023.114685.
Hu, W., Wang, Z.R., 2004. Deformation analyses of the integrated hydro-bulge forming of a spheroidal vessel from different preform types. J. Mater. Process. Technol. 151, 275–283. https://doi.org/10.1016/j.jmatprotec.2004.04.112.
Ifayefunmi, O., 2016. Buckling behavior of axially compressed cylindrical shells: comparison of theoretical and experimental data. Thin-Walled Struct. 98. https://doi.org/10.1016/j.tws.2015.10.027.
Ifayefunmi, O., Błachut, J., 2013. Instabilities in imperfect thick cones subjected to axial compression and external pressure. Mar. Struct. 33. https://doi.org/10.1016/j.marstruc.2013.06.004.
Jasion, P., Magnucki, K., 2015. Elastic Buckling of Cassini Ovaloidal Shells under External Pressure - Theoretical Study, vol. 67. Archives of Mechanics.
Kohnen, W., 2009. Human exploration of the deep seas: fifty years and the inspiration continues. Mar. Technol. Soc. J. 43. https://doi.org/10.4031/MTSJ.43.5.30.
Li, B., Pang, Y., jie, Cheng, xue, Y., Zhu, X. meng, 2017. Collaborative optimization for ring-stiffened composite pressure hull of underwater vehicle based on lamination parameters. Int. J. Nav. Archit. Ocean Eng. 9, 373–381. https://doi.org/10.1016/j.ijnaoe.2016.09.009.
Li, K., Zheng, J., Liu, S., Ge, H., Sun, G., Zhang, Z., Gu, C., Xu, P., 2019. Buckling behavior of large-scale thin-walled ellipsoidal head under internal pressure. Thin-Walled Struct. 141. https://doi.org/10.1016/j.tws.2019.04.031.
Liu, D., Zhu, H., Liu, F., Cao, J., Ding, Z., Zhang, Y., 2022a. Buckling failure analysis of PMMA spherical pressure hull. Ocean Eng. 245. https://doi.org/10.1016/j.oceaneng.2021.110465.
Liu, X., Zhang, J., Di, C., Zhan, M., Wang, F., 2022b. Buckling of hydroformed toroidal pressure hulls with octagonal cross-sections. Metals 12. https://doi.org/10.3390/met12091475.
Ma, Y.Q., Wang, C.M., Ang, K.K., 2008. Buckling of super ellipsoidal shells under uniform pressure. Thin-Walled Struct. 46. https://doi.org/10.1016/j.tws.2008.01.013.
Magnucki, K., Jasion, P., 2013. Analytical description of pre-buckling and buckling states of barrelled shells under radial pressure. Ocean Eng. 58, 217–223. https://doi.org/10.1016/j.oceaneng.2012.11.004.
Malinowski, M., Belica, T., 2017. Numerical Investigation of Buckling of Cassini Ovaloidal Sandwich Shells under External Pressure.
Pan, B., Cui, W., 2010. An overview of buckling and ultimate strength of spherical pressure hull under external pressure. Mar. Struct. https://doi.org/10.1016/j.marstruc.2010.07.005.

Pan, B.B., Cui, W.C., Shen, Y.S., 2012. Experimental verification of the new ultimate strength equation of spherical pressure hulls. Mar. Struct. 29. https://doi.org/10.1016/j.marstruc.2012.05.007.

Pan, B.B., Cui, W.C., Shen, Y.S., Liu, T., 2010. Further study on the ultimate strength analysis of spherical pressure hulls. Mar. Struct. 23. https://doi.org/10.1016/j.marstruc.2010.11.001.

Pan, B. bin, Cui, W.C., 2011. A comparison of different rules for the spherical pressure hull of deep manned submersibles. Chuan Bo Li Xue/Journal of Ship Mechanics 15.

Sowiński, K., Jasion, P., 2019. Strength and stability of shells based on Booth lemniscate loaded with external pressure. Thin-Walled Struct. 144. https://doi.org/10.1016/j.tws.2019.106284.

Standards Press of China, 2011. GB/T 228. 1-2010: Metallic Materials-Tensile Testing-Part 1: Method of Test at Room Temperature. Standards Press of China.

Tang, W. xian, Wang, W. min, Zhang, J., Wang, S. yan, 2019. Buckling of Cassini oval pressure hulls subjected to external pressure. China Ocean Eng. 33. https://doi.org/10.1007/s13344-019-0048-y.

Tang, Y., Zhang, J., Wang, F., Zhao, X., Wang, M., 2023. Buckling performance of ellipsoidal pressure hulls with stepwise wall thicknesses. Ocean Eng. 284. https://doi.org/10.1016/j.oceaneng.2023.115165.

Thompson, J.M.T., 2015. Advances in shell buckling: theory and experiments. International Journal of Bifurcation and Chaos. https://doi.org/10.1142/S0218127415300013.

Timoshenko, S.P., Gere, J.M., Prager, W., 1962. Theory of elastic stability. J. Appl. Mech. 29. https://doi.org/10.1115/1.3636481. Second.

Ventsel, E., Krauthammer, T., Carrera, E., 2002. Thin plates and shells: theory, analysis, and applications. Appl. Mech. Rev. 55. https://doi.org/10.1115/1.1483356.

Wang, Z.R., Hu, W.L., Yuan, S.J., Wang, X.S., 2018. Engineering plasticity: theory and applications in metal forming. J. Chem. Inf. Model. pp 345.

Wang, Z.R., Liu, G., Yuan, S.J., Teng, B.G., He, Z.B., 2005. Progress in shell hydroforming. J. Mater. Process. Technol. 167, 230–236. https://doi.org/10.1016/j.jmatprotec.2005.05.045.

Yuan, S.J., Hu, L., He, Z. Bin, Teng, B.G., Wang, Z.R., 2013. Research on Two-step Hydro-Bulge Forming of Ellipsoidal Shell with Larger axis Length Ratio, vol. 20. Journal of Harbin Institute of Technology, New Series.

Yuan, S.J., Zhang, W.W., Teng, B.G., 2015. Research on hydro-forming of combined ellipsoidal shells with two axis length ratios. J. Mater. Process. Technol. 219. https://doi.org/10.1016/j.jmatprotec.2014.12.015.

Yuan , S. J., Wang, Z.R., 1996. Research on the residual stresses of hydrobulged spherical vessels. J. Mater. Process. Technol. 58. https://doi.org/10.1016/0924-0136(95)02145-0.

Yuansong, Z., Shijian, Y., Fengzhi, W., Wang, Z.R., 1997. Research on the integral hydrobulge forming of ellipsoidal shells. J. Mater. Process. Technol. 72, 28–31.

Zhang, J., Cheng, P., Wang, F., Tang, W., Zhao, X., 2022a. Hydroforming and buckling of an egg-shaped shell based on a petal-shaped preform. Ocean Eng. 250. https://doi.org/10.1016/j.oceaneng.2022.111057.

Zhang, J., Dai, M., Wang, F., Tang, W., Zhao, X., 2021a. Buckling performance of egg-shaped shells fabricated through free hydroforming. Int. J. Pres. Ves. Pip. 193. https://doi.org/10.1016/j.ijpvp.2021.104435.

Zhang, J., Dai, M., Wang, F., Tang, W., Zhao, X., Zhu, Y., 2022b. Theoretical and experimental study of the free hydroforming of egg-shaped shell. Ships Offshore Struct. 17, 257–267. https://doi.org/10.1080/17445302.2020.1827637.

Zhang, J., Di, C., Wang, F., Tang, W., 2021b. Buckling of segmented toroids under external pressure. Ocean Eng. 239. https://doi.org/10.1016/j.oceaneng.2021.109921.

Zhang, Jian, Hua, Z., Tang, W., Wang, F., Wang, S., 2018a. Buckling of externally pressurised egg-shaped shells with variable and constant wall thicknesses. Thin-Walled Struct. 132, 111–119. https://doi.org/10.1016/j.tws.2018.08.013.

Zhang, J., Liu, X., Zhan, M., Wang, F., Zhao, X., 2022c. Hydroforming and buckling of toroids with polyhedral sections. Ships Offshore Struct. https://doi.org/10.1080/17445302.2022.2082106.

Zhang, J., Wang, Feng, Wang, Fang, Zhao, X., Tang, W., Chen, F., 2021c. Buckling properties of bulged barrels under external pressure. Thin-Walled Struct. 168. https://doi.org/10.1016/j.tws.2021.108226.

Zhang, J., Wang, M., Wang, W., Tang, W., Zhu, Y., 2017a. Investigation on egg-shaped pressure hulls. Mar. Struct. 52, 50–66. https://doi.org/10.1016/j.marstruc.2016.11.005.

Zhang, Jian, Wang, Weimin, Wang, F., Tang, W., Cui, W., Wang, Weibo, 2018b. Elastic buckling of externally pressurized Cassini oval shells with various shape indices. Thin-Walled Struct. 122, 83–89. https://doi.org/10.1016/j.tws.2017.10.008.

Zhang, J., Wang, W.M., Cui, W.C., Tang, W.X., Wang, F., Chen, Y., 2018. Buckling of longan-shaped shells under external pressure. Mar. Struct. 60. https://doi.org/10.1016/j.marstruc.2018.04.002.

Zhang, J., Wang, X., Tang, W., Wang, F., Zhu, Y., 2021d. Non-linear collapse behavior of externally pressurized resin toroidal and cylindrical shells: numerical and experimental studies. Ships Offshore Struct. 16. https://doi.org/10.1080/17445302.2020.1745546.

Zhang, Jian, Zhang, M., Cui, W., Tang, W., Wang, F., Pan, B., 2018c. Elastic-plastic buckling of deep sea spherical pressure hulls. Mar. Struct. 57. https://doi.org/10.1016/j.marstruc.2017.09.007.

Zhang, J., Zhang, M., Tang, W., Wang, W., Wang, M., 2017b. Buckling of spherical shells subjected to external pressure: a comparison of experimental and theoretical data. Thin-Walled Struct. 111. https://doi.org/10.1016/j.tws.2016.11.012.

Zhang, J., Zhu, Z., Wang, F., Zhao, X., Zhu, Y., 2021e. Buckling behaviour of double-layer and single-layer stainless steel cylinders under external pressure. Thin-Walled Struct. 161. https://doi.org/10.1016/j.tws.2021.107485.

Zhang, Jian, Liu, C., Tang, W., Wang, F., Zhao, X., Zhang, Jinfei, Tang, L., 2022d. Collapse of barreled frustums under external hydrostatic pressure. Mar. Struct. 84. https://doi.org/10.1016/j.marstruc.2022.103218.

Zhang, Q., Wang, Z.R., 2015. Shape improvement of a dieless hydro-bulged sphere made of hexagonal and pentagonal shaped panels. J. Mater. Process. Technol. 220, 87–95. https://doi.org/10.1016/j.jmatprotec.2015.01.012.

Zhang, W.W., Teng, B.G., Yuan, S.J., 2015. Research on deformation and stress in hydroforming process of an ellipsoidal shell without constraint. Int. J. Adv. Manuf. Technol. 76, 1555–1562. https://doi.org/10.1007/s00170-014-6368-4.

Zhang, W.W., Yuan, S.J., 2016. Research on hydro-forming of combined prolate ellipsoidal shell with double generating lines. Int. J. Adv. Manuf. Technol. 82, 595–603. https://doi.org/10.1007/s00170-015-7351-4.

Zheng, J., Zhang, Z., Li, K., Yu, Y., Gu, C., 2020. A simple formula for prediction of plastic collapse pressure of steel ellipsoidal heads under internal pressure. Thin-Walled Struct. 156. https://doi.org/10.1016/j.tws.2020.106994.

Zingoni, A., 2015. Liquid-containment shells of revolution: a review of recent studies on strength, stability and dynamics. Thin-Walled Struct. https://doi.org/10.1016/j.tws.2014.10.016.

Zingoni, A., Enoma, N., 2020. Strength and stability of spherical-conical shell assemblies under external hydrostatic pressure. Thin-Walled Struct. 146. https://doi.org/10.1016/j.tws.2019.106472.

Zoelly, R., 1915. Ueber ein Knickungsproblem an der Kugelschale, Zürcher & Furrer. https://doi.org/10.3929/ethz-a-000091951.